Structural Characterization and Thermal Properties of the Anti-malarial Drug: Lumefantrine

Pramod B. Pansuriya, Glenn E.M. Maguire and Holger B. Friedrich* [ID] §

School of Chemistry and Physics, University of KwaZulu-Natal, Westville Campus, Durban, 4000, South Africa.

ABSTRACT

The anti-malarial lumefantrine was characterized in the solid as well as the solution state. The solid state analysis was carried out by single crystal X-ray diffraction (SCXRD), powder X-ray diffraction (PXRD), DSC, TG-DTG and ATR-IR. The single crystal structure of lumefantrine has been solved. The structure is stabilized *via* inter- as well as intra-C–H…Cl interactions, intra hydrogen bonding O–H…N interactions and C–H…O weak interactions. The Hirshfeld surface intermolecular interactions have been studied using the crystal structure. Solution structure analyses have been done by NMR, COSY/NOESY, HSQC and mass spectrometry. The thermal properties were studied by solid-state differential scanning calorimetry and thermogravimetric analysis of the drug under nitrogen as well as in air.

KEYWORDS

Single crystal structure, lumefantrine, 2D NMR, DSC, PXRD.

1. Introduction

Malaria is a parasitic disease in humans, with transmission occurring in countries with a combined population of *c.* three billion people. It causes thousands of deaths each year.[1] The disease is caused by protozoan parasites of the genus *Plasmodium*. This malarial parasite depends on both mosquitoes and humans for its cycle. At the same time, growing levels of drug resistance have resulted in significant mortality worldwide and much evidence has emerged on the resistance of *Plasmodium falciparum* to many antimalarial agents.[2] Improving access to effective anti-malarial treatment is very important. In Africa and Asia, where the disease is most prevalent, limited health care infrastructure complicates efforts to predict clinical demand. As a result the combination of lumefantrine and artemether (Coartem and Riamet, Falcynate-LF) was developed as a fixed-dose combination therapy (ACT) for the treatment of acute uncomplicated 'Plasmodium falciparum malaria'. The combination is a potent, synergistically active and well-tolerated malaria treatment, powerful towards areas of multi-drug resistance.[3–5]

Both the individual drugs were developed in China. Lumefantrine (benflumetol or CGP 56695) is purely synthetic and was synthesized in the 1970s by the Academy of Military Medical Sciences, in Beijing. It was registered in China for anti-malarial use in 1987. The World Health Organization's (WHO) prequalified 'Coartem' in 2001 as a fixed dose combination therapy for efficacy, safety and quality. From 2002, this medication was adopted by the WHO and UN agencies.[6,7] Coartem is approved by the European Medicines Agency (EMA) and the U.S. Food and Drug Administration (FDA).

The oral drugs have a shelf life of only two years.[8] Much work is in progress to improve shelf life, novel drug release, and delivery systems. For these purposes, a molecular level study is necessary. In the present research we report the molecular level structural investigation, as well as the thermal decomposition of lumefantrine using single crystal X-ray diffraction (SCXRD), powder X-ray diffraction (PXRD), NMR, 2D NMR, DSC, TG-DTG and an ATR-IR study.

2. Experimental

2.1. Materials

The reagents and solvents were obtained from commercial sources in analytical grade. They were used without further purification. The melting point was recorded on an Ernst Leitz Wetzlar hot-stage microscope. It is uncorrected. Suitable crystals for X-ray diffraction were obtained at room temperature by slow evaporation using a mixture of dichloromethane and ethyl acetate.

2.2 Methods

2.2.1. *X-ray Diffraction Studies*

The crystal evaluation and data collection were done on a Bruker KAPPA APEXII DUO diffractometer using graphite-monochromated Mo Kα radiation (λ = 0.71073 Å) at 173(2)K. The reflections were successfully indexed by an automated indexing routine built into the *APEX*II program suite.[9] The program *SAINT+* was used for data reduction.[10] The data were scaled and absorption correction performed using SADABS. The structure was solved by direct methods using *SHELXS* and refined by the full-matrix least-squares method based on F^2 using SHELXL-97.[11] Non-H atoms were first refined anisotropically. The program Olex2 was used to prepare molecular graphic images.[12] All H atoms, except H1, were placed in idealized positions and refined in riding models with U$_{iso}$ assigned to 1.2 or 1.5 times the values of their parent atoms and constraint distances of C-H ranging from 0.95 Å to 1.00 Å. The hydrogen H1 was located in the electron difference maps and refined with the simple bond constraint d(O1-H1) = 0.970(5) Å.

The PXRD pattern of the powder samples was obtained at room temperature using a Bruker D8 Advance diffractometer with Cu Kα radiation (1.54 nm), at 40 kV and 40 mA. Accurately weighed 300 mg of powder was loaded in a 25 mm poly-methyl methacrylate (PMMA) holder and gently pressed using a clean glass slide to ensure coplanarity of the powder surface with the

RESEARCH ARTICLE

P.B. Pansuriya, G.E.M. Maguire and H.B. Friedrich,
S. Afr. J. Chem., 2019, **72**, 253–262,
<https://journals.co.za/content/journal/chem/>.

254

surface of the holder. The diffractogram was obtained in continuous mode, step size = 0.01 ° and step time = 0.5 s over the 2θ angular range of 15–90 °.

2.2.2. *NMR Spectroscopy*

^{1}H NMR, ^{13}C NMR, NOESY, HSQC and COSY spectra were obtained using a Bruker Avance 400 MHz NMR spectrometer in CDCl$_3$.

2.2.3. *Differential Scanning Calorimetry (DSC) and Thermogravimetric Analysis (TG)*

DSC and TG experiments were carried out with a TA Instruments SDT Q600 V20.9 and Universal Analysis 2000 software (version 4.5A). A standard calibration process for the TG-DSC experiments was carried out with an empty pan, zinc (T_{fusion}: 419.5 °C) and sapphire standards to correct the baseline, temperature and heat flow, respectively. Accurately weighed samples in crimped aluminium pans were thermally scanned from 30 °C to 900 °C, heating at a rate of 10.0 °C min^{-1}. A dry nitrogen purge was maintained at 10 mL min^{-1}. The experiment was repeated by purging air at 10, 15, 20, 25 mL min^{-1} to examine aerial oxidation with respect to temperature. Before testing, the instrument calibration was checked using a sample of calcium oxalate monohydrate according to ASTM norms.

2.2.4. *IR (ATR) Spectroscopy and Mass Spectrometry*

The Fourier transformed infrared spectra were recorded *via* attenuated total reflectance (ATR) using a Perkin Elmer Universal spectrometer. A Waters Micromass LCT Premier TOF-MS was used to attain the mass spectrum.

3. Results and Discussion

3.1. Single Crystal Structure Analysis and Hirshfeld Surface Analysis

The single crystal X-ray study of lumefantrine was carried out using crystals grown in a mixture of solvents. The crystal data are summarized in Table 1.

The Olex view of the lumefantrine molecule, presented in Fig. 1A, indicates that the fluorene rings are in the same plane and a little tilted on both ends. In Fig. 1B, the asymmetric unit of lumefantrine shows inter- as well as intramolecular C–H…Cl interactions, also molecular intra hydrogen bonding O–H…N interaction and C–H…O weak interactions. Due to the alternate

Table 1 Crystal data of lumefantrine.

Parameters	Lumefantrine
Formula	C$_{30}$H$_{32}$Cl$_3$N O
Mol. mass	528.92
Temperature/K	173
Radiation (Å) MoKa	0.71073
Crystal system	Monoclinic
Space group	P$_{21}$
a/Å	8.8019(6)
b/Å	9.4406(6)
c/Å	15.8201(11)
α/°	90
β/°	95.497(2)
γ/°	90
Volume/Å^3	1308.53(15)
Z	2
Calculated density/g cm^{-3}	1.342
Mu(MoKa)/mm^{-1})	0.375
F(000)	556
Crystal size /mm^3	0.09 × 0.17 × 0.20
θ Min–Max/°	2.3, 28.3
Dataset	–11: 11 ; –12: 12; –14: 21
Tot., uniq. data, R_{int}	11590, 6499, 0.023
Observed data [I > 2.0σ(I)]	5731
Nref, Npar	6499, 322
R, wR2, S	0.0374, 0.0860, 1.03
Min. and max. resd. dens./e Å^{-3}	–0.20, 0.27
No. of C–X…π interactions	2
No. of π…π interactions	18

C–H…Cl interactions, the molecules expand the lattice through the *b* as well as *c* axes, in the *a*-axis it makes chains, whilst in the *b*-axis it makes networks. There are in total 18 π…π interactions, which cause a zigzag ladder-like structure in the *c*-axis. The hydrogen bonding and weak interactions of lumefantrine are listed in Table 2.

Hirshfeld surfaces, examining fingerprint plots, were created by *CrystalExplorer 2.1* software which can recognize the types and regions of the intermolecular interactions, and the proportion of this interaction. The molecular Hirshfeld surface in the crystal structure is accumulated from the electron distribution. Hirshfeld surfaces of the compound have been mapped over d_{norm} and electrostatic potential (Fig. 2). The normalized contact distance (d_{norm}) is based on both d_e, d_i and the van der Waals
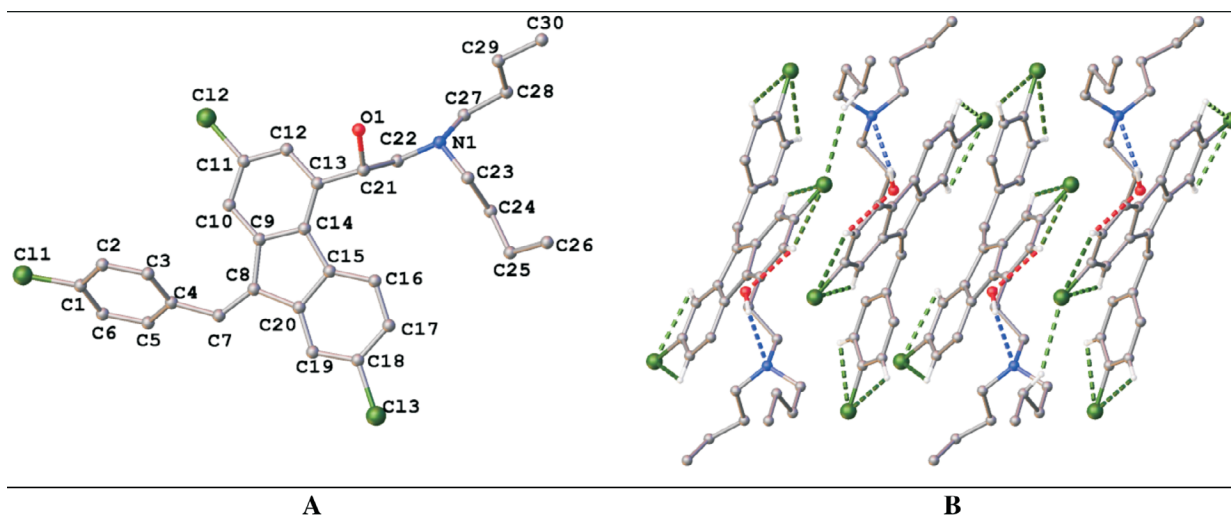

Figure 1 (**A**) Represents the asymmetric unit of the lumefantrine, whilst (**B**) represents the C–H—O, C–H—N, C–H—Cl interactions in packing.

Table 2 Hydrogen bonding and weak interactions of lumefantrine.

Donor–H….Acceptor	D–H	H…A	D…A	D–H…A	Bonding
O(1)–H(1)…N(1)	0.96(3)	2.20(2)	2.767(2)	116(2)	H-bonding
C(22)–H(22B)…Cg(2) [a]	0.768	2.95	3.718(2)	135	C–H…Cg
C(11)–Cl(2)…Cg(1) [b]	1.102	3.5919(10)	4.694(2)	119.07(7)	C–Cl…Cg

[a] Symmetry transformations used to generate equivalent atoms: 1-X,1/2+Y,-Z; [b] 1-X,1/2+Y,-Z.
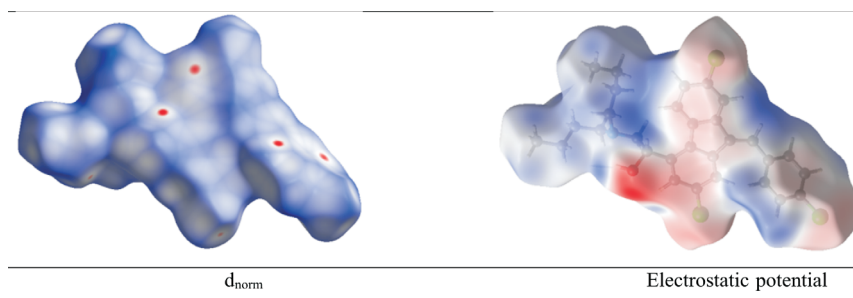
Figure 2 d_{norm} and electrostatic potential of lumefantrine.

(vdw) radii of the atom, as listed in Equation 1. The 2D fingerprint plot is the combination of de and d_i, where d_e is the distance from the point to the nearest nucleus external to the surface, while d_i is the distance to the nearest nucleus internal to the surface. The value of d_{norm} is negative or positive when intermolecular contacts are shorter or longer than the van der Waals separations, respectively. The interactions between functional groups are shown as deep red areas in the Hirshfeld surfaces. Slight red areas on the surface correspond to weaker and longer contacts than the hydrogen bonds. Visible spots are attributed to the H⋯H contacts. The normalized distance (d_{norm}), based on d_e and d_i, is given by Equation 1.

$$d_{norm} = (d_i - r_i^{vdw})/r_i^{vdw} + (d_e - r_e^{vdw})/r_e^{vdw} \qquad (1)$$

where r_i^{vdw} and r_e^{vdw} are the van der Waals (vdw) radii of the atoms.

The result obtained from the Hirshfeld surface of lumefantrine is shown in Fig. 3. The inter- and intramolecular H⋯O/O⋯H interactions between C–H and the hydroxyl group oxygen with a 2.6% proportion appear as short spikes in the 2D fingerprint plot. The 2.8% C⋯Cl contribution between carbon and chlorine appears as a scissor wing in the centre. C–H…π interactions are present because the two-dimensional fingerprint plot shows two pairs of typical 'wings' at the top left and bottom right.

The wings at the bottom right ($d_e > d_i$) correspond to the surface around the acceptor, whereas those at the top left ($d_i < d_e$) are due to points on the surface around the C–H donor. Herein, for all C–H…C interactions, C–H…π appear in the fingerprint plot as a characteristic style of C⋯C bond contacts, comprising 3.3%. C…H/H⋯C contacts make up 20.0% of the total Hirshfeld surface area. The inter- and intramolecular C–H⋯Cl interactions between C–H and chlorine, with a 25.9% proportion, is seen as short spikes in the 2D fingerprint plot.

3.2. Powder X-ray Diffraction

The powder X-ray diffraction pattern of lumefantrine is shown in Fig. 4. The compound shows a wide range of reflections ranging from $2\theta = 10\,°–50\,°$. The compound shows a pattern that corresponds to a single crystalline phase. The peaks are sharp, which shows the crystalline nature of the molecule. The powder X-ray pattern matches the single crystal powder patterns. The resultant lattice parameters are summarized in Table 3.

3.3. NMR Spectroscopy

Examination of the ^{1}H-NMR spectrum of lumefantrine (Fig. 5) confirmed the presence of the hydroxyl group at 4.51 ppm as a singlet, which corresponds to one proton. The H21 proton appears as a dd at 5.35, which corresponds to one proton. The four N-CH$_2$ protons appear at 2.47–2.72 ppm as a multiplet. The CH$_2$ protons of carbons 25, 28 and 26, 29 give signals between 1.33–1.40 and 1.45–1.51 ppm, respectively. Each signal is seen as a multiplet and corresponds to four protons. The CH$_3$ protons appear at 0.96 as a triplet corresponding to six protons.

^{13}C DEPT, COSY, NOESY and HSQC was used to confirm assignment of protons. The 2D NMR spectra (ESI), assignments

Table 3 The lattice parameters from powder and single crystal XRD.

2θ	d/Å	h	k	l
11.37	7.78	0	0	2
13.74	6.44	1	1	0
14.52	6.10	0	1	2
15.32	5.78	1	1	1
16.31	5.44	1	0	2
17.14	5.17	1	1	–2
18.32	4.84	1	1	2
20.25	4.39	2	0	0
20.44	4.35	2	0	–1
21.28	4.18	2	1	0
22.33	3.98	2	1	0
23.32	3.82	2	1	1
24.32	3.66	0	1	4
25.80	3.45	2	1	2
26.60	3.35	1	2	–3
27.52	3.24	1	1	4
28.68	3.11	2	2	1
29.46	3.03	2	1	3
31.73	2.82	3	0	1
33.24	2.70	0	3	3
37.15	2.42	3	2	1
39.66	2.27	1	2	–6
43.11	2.10	4	0	–3
44.50	2.04	2	1	–7
46.00	1.97	0	0	8
49.70	1.83	3	1	–7
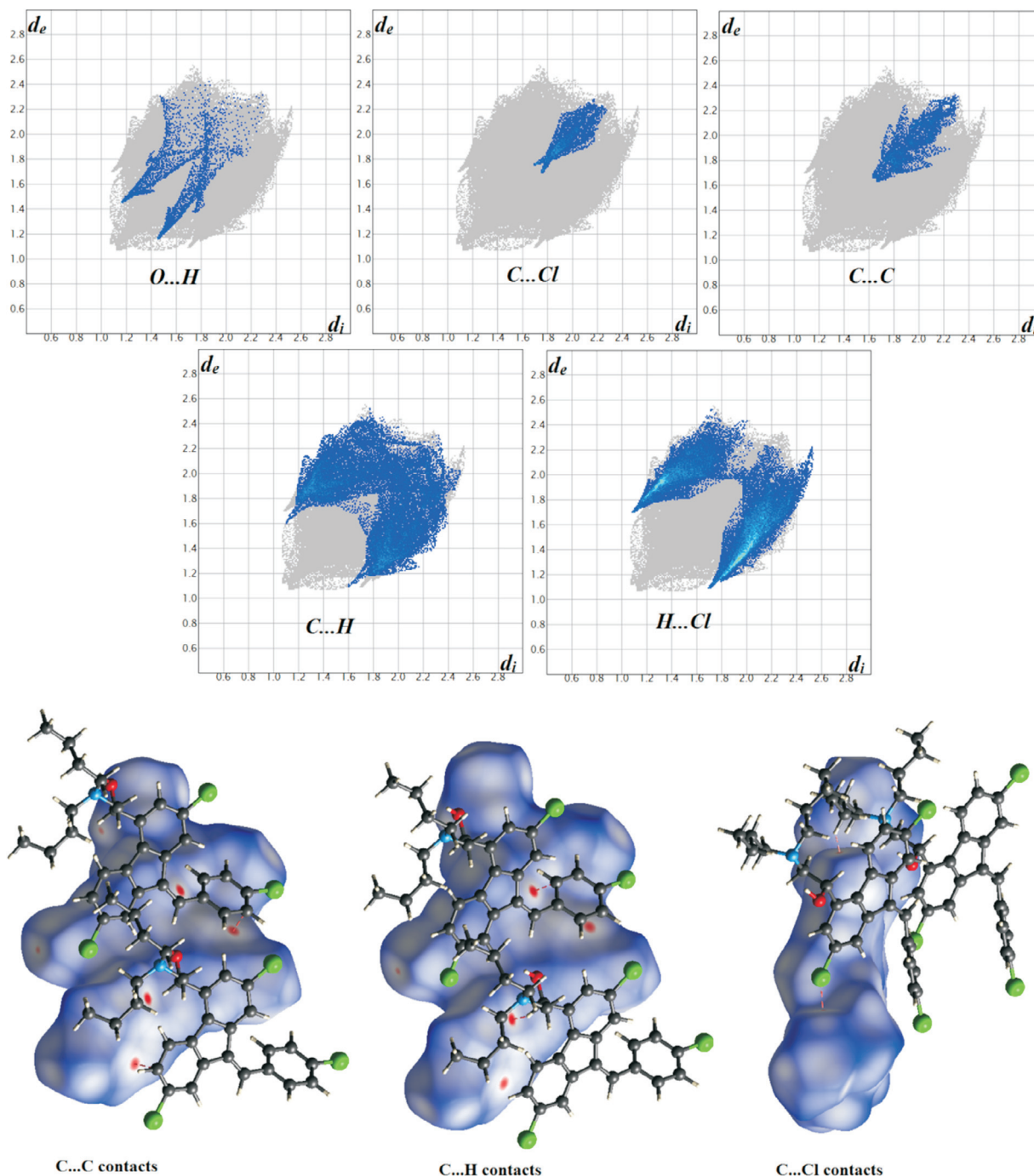
Figure 3 Fingerprint plots of lumefantrine contacts, resolved into different intermolecular interactions contributing to the total Hirshfeld surface area of the molecules.

are given in Table 4. Thus protons H16, 17, 19, 20 are seen at 7.43–7.47 ppm as multiplets as correlated by COSY, whilst the aromatic protons H16 and 20 correlates to H14 *via* NOE. A relationship was seen between H6, H12 and H21. Further correlations were found between the dibutylamine ring protons H12 and the *N*-methyl protons H22.

3.4. Thermal Analysis

The thermogravimetric (TG) analyses plots of the lumefantrine powder, that were obtained under air with different heating rates can be seen in Fig. 8. Table 5 shows the TG results for the decomposition of lumefantrine, and includes decomposition temperatures, mass loss, and peak temperatures of the DSC and TG analyses.

Lumefantrine did not show loss of water content up to 132 °C (its melting temperature) in the TG traces in Fig. 6. It is confirmed that its decomposition does not occur directly after its melting. One can easily observe in the inert environment, decomposition after the melting point in a first step, giving a 16.1% mass loss, followed by a 16.9% loss. The third step loss of 23.7% leaves behind 29.1% mass. In the case of decomposition in air, the first step gives a 42.1% loss, followed by a 51.0% loss, leaving behind only 6.4%.

The thermogravimetric analyses results are expressed as a function of conversion α, which is defined in Equation 2.[13] The mass loss phenomenon is closely related to the nature of the compound (Fig. 7), because thermal decomposition is directly related to the stability of the compound.

Table 4 ¹H-NMR, ¹³C-NMR and 2D NMR assignment of lumefantrine.

Carbon	¹³C NMR	Proton	¹H NMR	COSY	NOESY	HSQC
1	130.7	H1	7.44(H, m, 7.43–7.47)	–	–	H1
2	134.3	–	–	–	–	–
3	126.5	H6	7.67(H, m, 7.67–7.67)	–	H21	–
4	138.4	–	–	–	–	–
5	136.6	–	–	–	–	–
6	120.8	H3	7.71(H, m, 7.71–7.72)	–	–	–
7	135.1	–	–	–	–	–
8	140.0	–	–	–	–	–
9	133.0	–	–	–	–	–
10	127.8	H10	7.58(H, m, 7.56–7.60)	–	–	–
11	133.3	–	–	–	–	–
12	124.1	H12	7.58(H, m, 7.56–7.60)	–	H21	–
13	141.7	–	–	–	–	–
14	128.5	H14	7.31(H, m, 7.30–7.32)	–	H16, 20	–
15	135.1	–	–	–	–	–
16, 20	130.7	H16, 20	7.44(2H, m, 7.43–7.47)	H17, 19	H14	–
17, 19	129.2	H17, 19	7.44(2H, m, 7.43–7.47)	H16, 20	H14	–
18	134.8	–	–	–	–	–
21	65.6	H21	5.35(H, dd, J=4.3)	H22	H6, 12	H21
22	60.1	H22,	2.44(H, m, 2.41–2.44), 2.87(H, m, 2.85–2.89)	H21	H23, 24	H22
23, 24	53.5	H23, 24	2.59(4H, m, 2.47–2.72)	H25, 28	H22, 26, 29	H23, 24
25, 28	29.2	H25, 28	1.49(4H, m, 1.45–1.51)	H23, 24, 26, 29	H27, 30	H25, 28
26, 29	20.7	H26, 29	1.36(4H, m, 1.33–1.40)	H27, 30, 25, 28	H23, 24	H26, 29
27, 30	14.2	H27, 30	0.96(6H, t, J=7.2)	H26, 29	H25, 28	H27, 30

$$\alpha = \frac{M_0 - M}{M_0 - M_\infty} \quad (2)$$

where M is the actual mass of sample; M_0 is the initial mass of sample and M_∞ is the final mass of the sample.

The TG curves show a two-step decomposition pattern. As the heating rate increased, the onset temperature of the DTG curves and the peak temperature increased. These temperature shifts may be due to heat transfer. This might be due to rapid pyrolysis, which requires very high rates of heating and short residence times of reactant and products. The activation energies for thermal degradation were determined according to the Flynn and Wall and Ozawa (FWO) and Kissinger-Akahira-Sunose (KAS) methods.[14–19]

The rate of degradation of sample, $d\alpha/dt$, depends on the mass
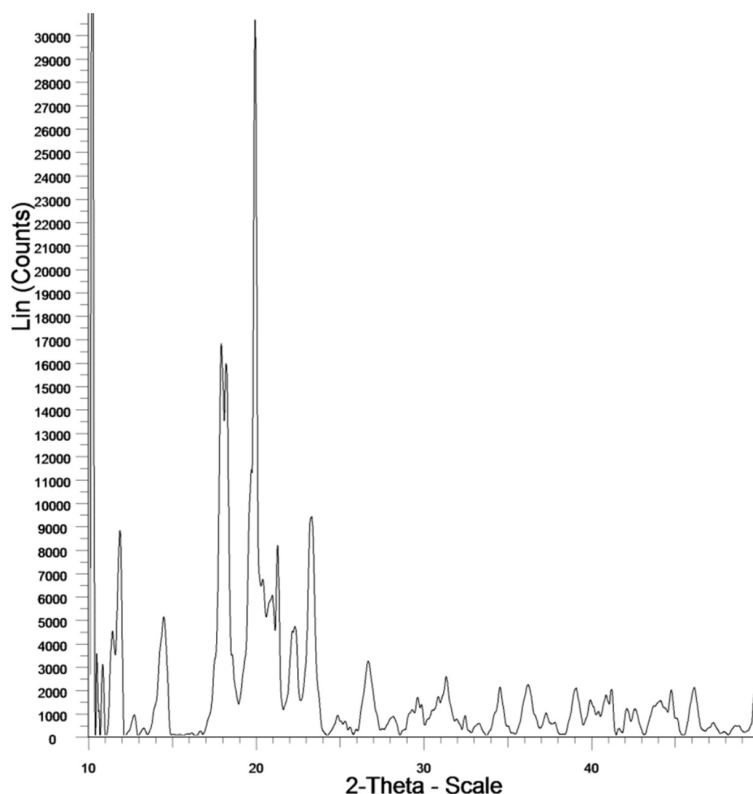
Figure 4 Powder X-ray pattern of lumefantrine.

RESEARCH ARTICLE

P.B. Pansuriya, G.E.M. Maguire and H.B. Friedrich,
S. Afr. J. Chem., 2019, **72**, 253–262,
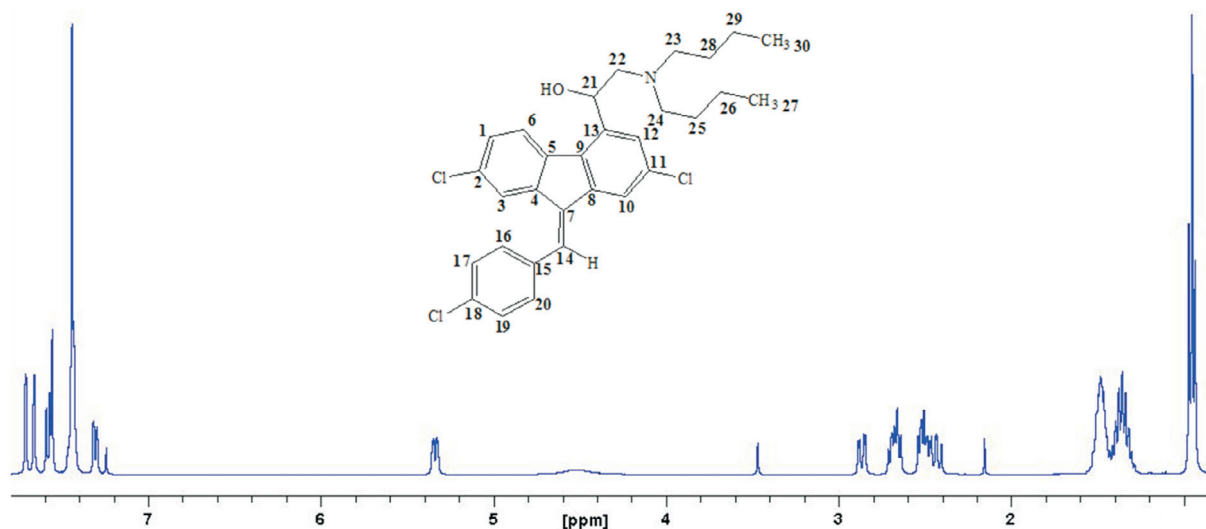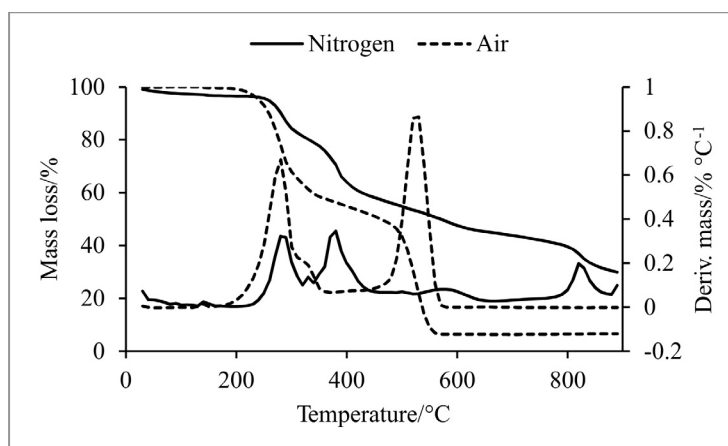<https://journals.co.za/content/journal/chem/>.

258

Figure 5 ^{1}H NMR spectrum of lumefantrine.

Figure 6 TG-DTG of lumefantrine in nitrogen.

of sample and temperature. This is expressed as shown in Equation 3:

$$\frac{d\alpha}{dt} = kf(\alpha) \tag{3}$$

where k is the rate constant and $f(\alpha)$ is the conversion functional relationship, and $f(\alpha)$ is the proportional to the decomposition of non-degraded or un-reacted material.

The temperature dependence of the rate constant k may be described by the Arrhenius expression (Equation 4):

$$k = A\exp\left(\frac{E_a}{RT}\right) \tag{4}$$

Combining equations (3) and (4) gives the overall rate of loss of reactive materials as:

$$\frac{d\alpha}{dt} = Af(\alpha)\exp\left(-\frac{E_a}{RT}\right) \tag{5}$$

The Flynn and Wall and Ozawa (FWO) method determines activation energy from the temperature *versus* mass loss data obtained at different heating rates, Equation 6:

$$\ln \beta = \left[\ln \frac{AE_a}{R} - \log(g(\alpha)) - 5.33\right] - 1.052 \ln\left(\frac{E_a}{RT}\right) \tag{6}$$

where β is the heating rate.

Should the degradation process mechanism be independent of the heating rate, then at constant α, $g(\alpha)$ is constant. Then the activation energy (E_a) is obtained from the slope of the linear equation, by plotting $\ln \beta$ against 1000/T at a particular conversion. Fig. 8 shows the FWO plot of degradation of lumefantrine.

The Kissinger-Akahira-Sunose (KAS) method is an isoconversion method and the activation energy can be calculated *via* Equation 7, to give Fig. 9.

Table 5 Thermo analytical data of lumefantrine at different heating rates under air.

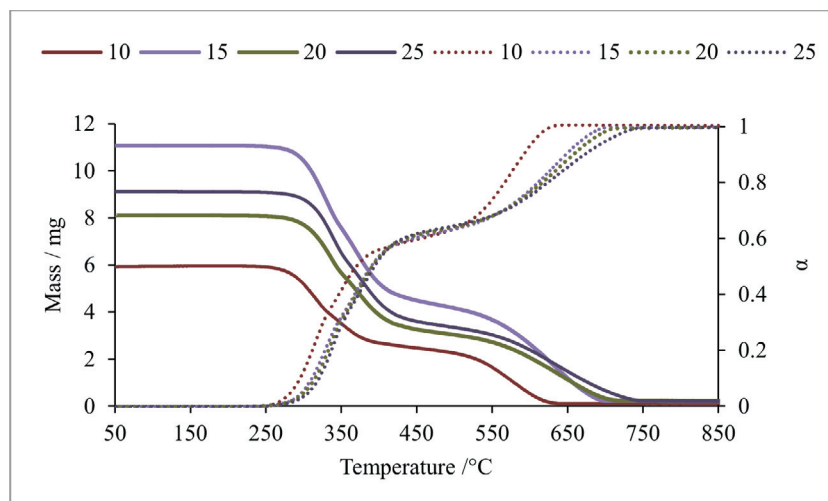| Heating rate °C min^{-1}	TG-DTG				Residue %	DSC		
	Stage 1		Stage 2			mp	Stage 1	Stage 2
	T_P	% loss	T_P	% loss		T_m	T_P	T_P
10	317.4	56.5	575.1	38.4	1.8	136.8	337.6	585.4
15	329.4	49.2	636.2	21.9	1.9	138.8	347.6	626.2
20	335.4	46.0	638.9	31.8	2.9	140.0	353.3	630.6
25	339.0	55.0	641.0	24.0	2.5	141.8	360.3	686.8

Figure 7 TG and conversion-α curve of lumefantrine in air at different heating rates.
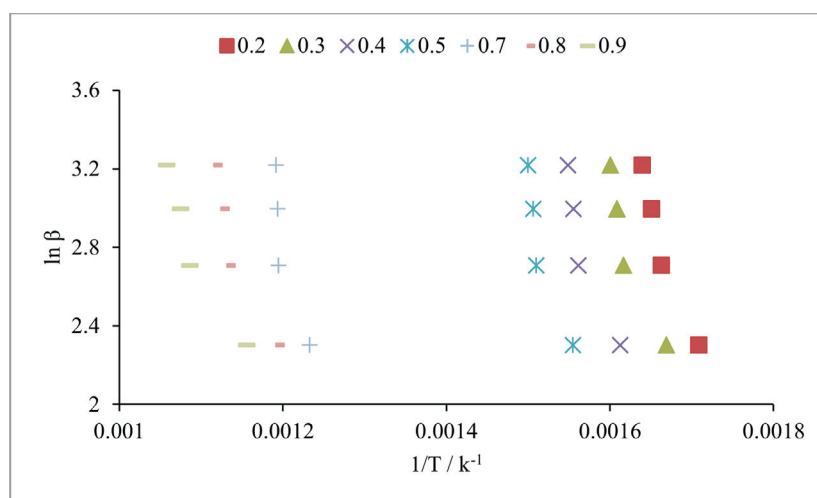

Figure 8 FWO plot for decomposition of lumefantrine.

$$\ln\left(\frac{\beta}{T^2}\right) = \left(\ln\frac{AR}{g(\alpha)E}\right) - \frac{E_a}{RT} \qquad (7)$$

The activation energies determined *via* the FWO and KAS methods are given in Table 6. The results for stage 1 decomposition are fairly compatible with each other, whilst those for stage 2 are less so. Both the methods are isoconversion methods by integral equations and show the same trends. The activation energy values from the KAS method are somewhat lower than the values from the FWO method. This may be because the KAS method is more valid for conversion-α value $20 \leq \alpha \leq 50$, which is only applicable for the step 1 degradation here.

The DSC curves under nitrogen as well as in air for lumefantrine are shown in Fig. 10. Small peaks represent endo(49.1 °C)-endo(132.2 °C)-exo(196.5 °C)-endo(257.6 °C) events under nitrogen, whilst the exo(51.6 °C)-endo(134.7 °C)-exo (293.5 °C)-endo(459.2 °C) in air is quite different and is associated with the crystallinity of the compound. The DSC trace endo peak

(459.2 °C), followed by an exo peak (522.4 °C) of the lumefantrine confirmed the complete decomposition process in air. Since the exo peak at 522.4 °C in air shows a high temperature degradation pattern that is different than what occurred under nitrogen; we can assume reactive species in the latter case may react with oxygen from air. These calorimetric results support the PXRD data confirming that lumefantrine is crystalline.

Figure 11a shows the DSC curves of lumefantrine and the corresponding DSC data are tabulated in Table 5. Fig. 11a shows that the peak associated with thermal decomposition moves up with increasing heating rate. The DSC curves in Fig. 11b show endo-exo-endo behaviour in the approximate temperature range of 250–450 °C between the two forms.

This is because lumefantrine undergoes the first degradation step with multiple polymorphic forms, which have different melting points. These could undergo reversible solid to solid transitions. Should the temperature reach the crystalline trans-

Table 6 Calculated activation energies from the FWO and KAS.

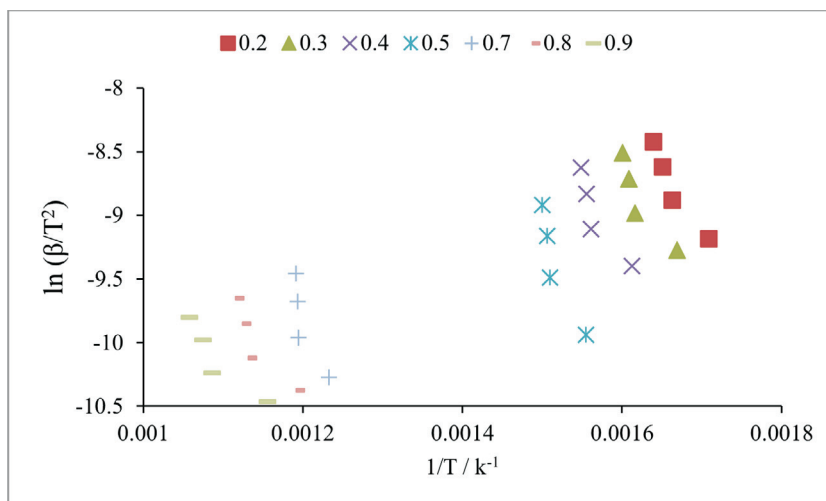| Compounds	Conversion α								
	0.2	0.3	0.4	0.5	Average kJ mol⁻¹	0.7	0.8	0.9	Average kJ mol⁻¹
	Stage 1					Stage 2			
FWO	99.9	95.1	99.6	114.9	102.4	139.0	84.6	69.6	97.7
KAS	86.8	81.7	86.3	135.0	97.4	125.7	67.9	51.7	81.8

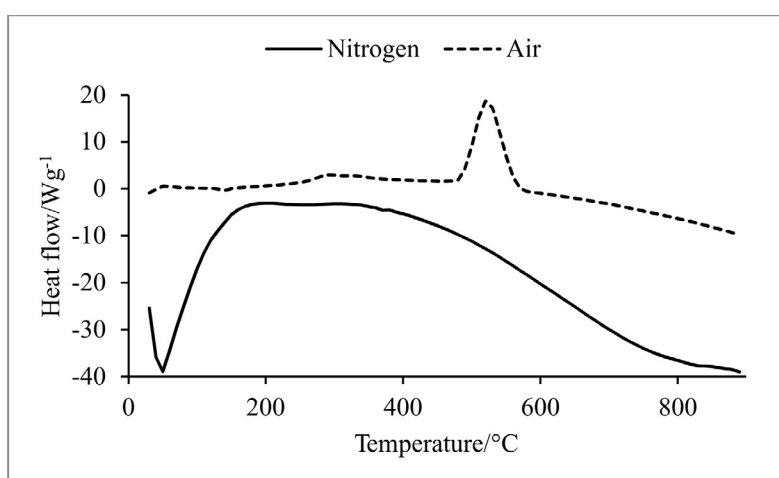**Figure 9** KAS plot for decomposition of lumefantrine.

Figure 10 DSC of lumefantrine in nitrogen.

formation temperature under linear heating conditions, the one polymorph could be transformed to another polymorph. This polymorph transformation process produces exothermic/endothermic effects.

The activation energy variation also supports the results obtained from DSC. There is a solid to solid transition in the stage 1 decomposition adduct which has lower activation energy lower than that of observed in the stage 2 decomposition. The activation energy values for α: 0.7, 0.8, and 0.9 vary, and from the DSC data it is seen that there are transformations of polymorphs in the decomposition process.

The exothermic peak due to crystalline transformation is very weak and easily masked by the endothermic peak due to melting at a rapid heating rate. Hence, there is only one clear endo-
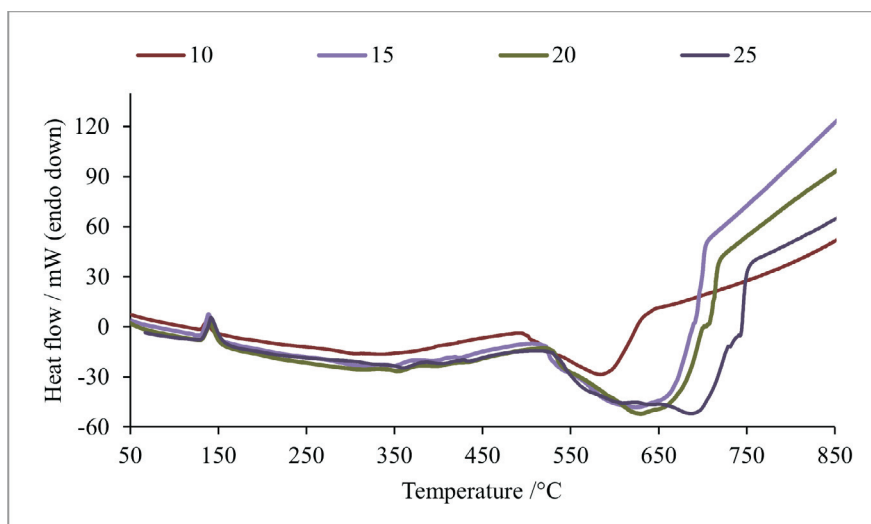
Figure 11a DSC of lumefantrine in air at different heating rates.
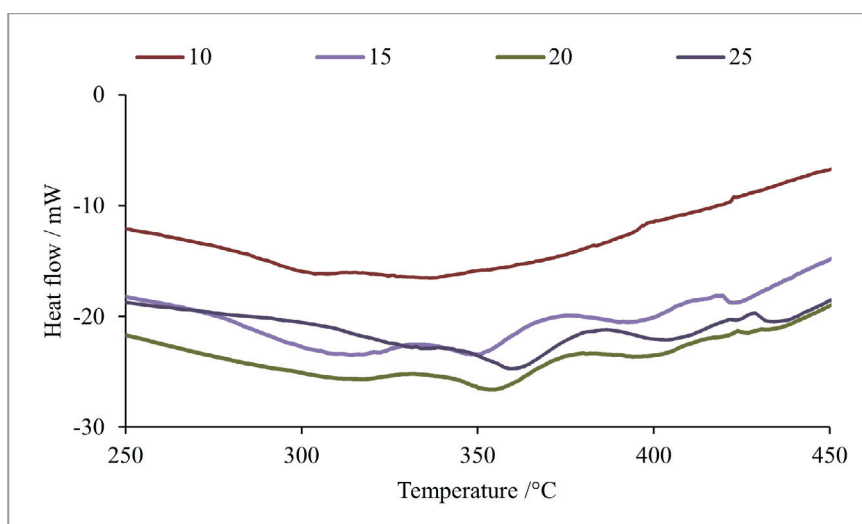
Figure 11b DSC of lumefantrine in air at different heating rates.
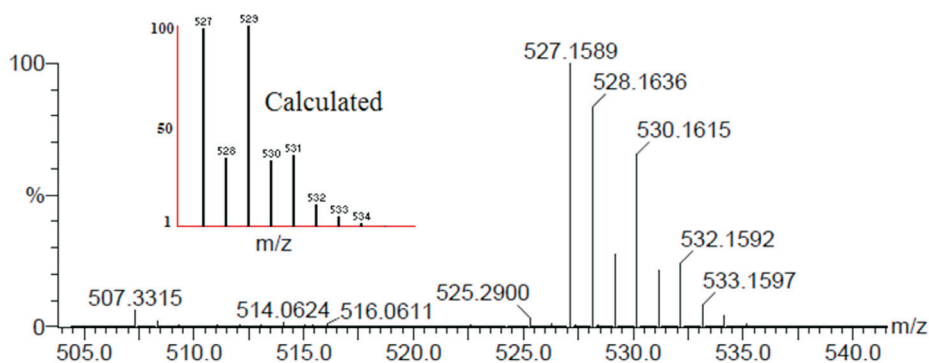
Figure 12 HRMS of lumefantrine.

thermic peak in the curve at 10 °C min^{-1}. A small shoulder precedes the second step decomposition endothermic on the 15–25 °C min^{-1} curve, while there is no shoulder peak on the 10 °C min^{-1} curve, probably due to the thermal decomposition mechanism and heating rate.

3.5. IR Spectroscopy (ATR) and Mass Spectrometry

In the FTIR spectra, characteristic bands are seen at 3392.2, 2950.2, 2927.0, 2870.0, 1863.88, 1752.32, 1634.3, 1588.45, 1485.6, 1463.5, 1442.5, 1397.0, 1365.3, 1339.9, 1307.7, 1267.5, 1172.7, 1155.6, 1097.7, 1087.5, 1069.9, 1013.5, 932.8, 872.6, 839.3, 805.2, 769.6, 752.1, 696.1, 654.9, 559.8, 521.5 cm^{-1}.

Thus, the IR spectrum of pure lumefantrine showed characteristic sharp peaks of alkane stretching/bending (-CH$_3$, -CH$_2$ and -CH) vibrations at ~1365.3, ~1485.6, ~2870.0 and ~2927.0 cm^{-1}. It also exhibited a C-O stretch at ~1172.7 cm^{-1} and a peak due to saturated hydroxyl O-H bending at ~3392.2 cm^{-1}. A selective stretching vibration at ~1155.6 cm^{-1} for the tertiary amine was also observed. Most of the peaks observed in the spectral region 769–872 cm^{-1}, 559–696 cm^{-1}, and 839–1013 cm^{-1} are due to bending of C-H, as well as -CH$_2$ and -CH deformation.

The mass spectrum of lumefantrine (Fig. 12) shows prominent m/z peaks of M-1: 527.15, M: 528.16, M+2:530.16 and M+4: 532.15 amu. The obtained mass spectrum is well matched with the calculated one (inset) and the profile shows the chlorine isotopes.

4. Conclusion

The structure of lumefantrine has been determined in solution and solid state using SCXRD, PXRD, NMR, DSC, TG and IR. The single crystal structure helped to understand the molecular interactions. PXRD patterns show that the drug has a single crystalline phase. The Hirshfeld surface analysis has helped to understand the contribution of intermolecular interactions on the surface of the molecular crystal. Thus using the SCXRD result, the maximum surface area of the molecule is occupied by C–H…Cl interactions. The thermal studies of the compound helped to confirm the melting process and thermal stability. Hence, TG shows a stepwise degradation process. It is concluded that aereal oxidative degradation of the drug may be low up to 325 °C, but at high temperature it decomposes rapidly. The results reported here may be useful for the development and modification of synthetic processes, new formulations and the further study of physicochemical properties of lumefantrine.

§ORCID iD

H.B. Friedrich: iD   orcid.org/0000-0002-1329-0815

References

1 World Health Organization, 2011, http://www.who.int/malaria/publications/world_malaria_report_2012/report/en/index.html

2 J.D. Maguire, I.W. Sumawinata, S. Masbar, B. Laksana, P. Prodjodipuro, P. Sismadi, N. Mahmud, M.J. Bangs, J.K. Baird and I. Susanti, Chloroquine-resistant *Plasmodium malariae* in south Sumatra, Indonesia, *Lancet*, 2002, **360**, 58–60.

3 S. Abdulla, I. Sagara, S. Borrmann, U. D'Alessandro, R. González, M. Hamel, B. Ogutu, A. Mårtensson, J. Lyimo, H. Maiga, P. Sasi, A. Nahum, Q. Bassat, E. Juma, L. Otieno, A. Björkman, H.P. Beck, K. Andriano, M. Cousin, G. Lefèvre, D. Ubben and Z. Premji, Efficacy and safety of artemether-lumefantrine dispersible tablets compared with crushed commercial tablets in African infants and children with uncomplicated malaria: a randomised, single-blind, multicentre trial. *Lancet*, 2008, **372**, 1819–1827.

4 M. van Vugt, S. Looareesuwan, P. Wilairatana, R. McGready, L. Villegas, I. Gathmann, R. Mull, A. Brockman, N.J. White and F. Nosten, Artemether-lumefantrine for the treatment of multidrug-resistant falciparum malaria, *Trans. R. Soc. Trop. Med. Hyg.*, 2000, **94**, 545–548.

5 E.A. Mueller, M. van Vugt, W. Kirch, K. Andriano, P. Hunt and P.I. de Palacios, Efficacy and safety of the six-dose regimen of artemether-lumefantrine for treatment of uncomplicated Plasmodium falciparum malaria in adolescents and adults: a pooled analysis of individual patient data from randomized clinical trials, *Acta Trop.*, 2006, **100**, 41–53.

6 World Health Organization, 2008, http://healthtech.who.int/pq/

7 World Health Organization, 2008, http://healthtech.whoz.int/pq/lists/mal_suppliers.pdf

8 R. Bate, R. Tren, K. Hess and A. Attaran, Physical and chemical stability of expired fixed dose combination artemether-lumefantrine in uncontrolled tropical conditions, *Malar. J.*, 2009, **8**, 1–7.

9 G. Sheldrick, A short history of SHELX, *Acta Crystallogr.*, *Sect. A: Found. Crystallogr.*, 2008, **64**, 112–122.

10 SAINT, Bruker AXS Inc. , Madison, WI, USA, 2006.

11 G.M. Sheldrick, SHELXS-97, SHELXL-97 and SADABS version 2.05, University of Göttingen, Germany, 1997.

12 O.V. Dolomanov, L.J. Bourhis, R.J. Gildea, J.A.K. Howard and H. Puschmann, OLEX2: a complete structure solution, refinement and analysis program, *J. Appl. Crystallogr.*, 2009, **42**, 339–341.

13 B. Janković, S. Mentus and M. Janković, A kinetic study of the thermal decomposition process of potassium metabisulfite: estimation of distributed reactivity model, *J. Phys. Chem. Solids*, 2008, **69**, 1923–1933.

14 T. Ozawa, A new method of analyzing thermogravimetric data, *Bull. Chem. Soc. Jpn.*, 1965, **38**, 1881–1886.

15 J.H. Flynn and L.A. Wall, General treatment of the thermogravimetry of polymers, *J. Res. Nat. Bur. Stand.*, 1966, **70**, 487–523.

16 T. Ozawa, Kinetic analysis of derivative curves in thermal analysis, *J. Therm. Anal.*, 1970, **2**, 301–324.

17 T. Akahira and T. Sunose, Method of determining activation deterioration constant of electrical insulating materials, *Res. Rep. Chiba Inst. Technol. (Sci. Technol.)*, 1971, **16**, 22–31.

18 M. Ak, G. Çılgı, F. Kuru and H. Cetişli, Thermal decomposition kinetics of polypyrrole and its star shaped copolymer, *J. Therm. Anal. Calorim.*, 2013, **111**, 1627–1632.

19 S. Söyleyici and G. Çılgı, Thermal and kinetic analyses of 2,5-bis(2-hydroxyphenyl)thiazolo[5,4-d]thiazole, *J. Therm. Anal. Calorim.*, **2014**, 705–709.

Structural characterizations and thermal properties of the anti-malarial drug: Lumefantrine

Pramod B. Pansuriya, Glenn E. M. Maguire, Holger B. Friedrich*

School of Chemistry and Physics, University of KwaZulu-Natal, Westville Campus, Durban
4000, South Africa
*E-mail: friedric@ukzn.ac.za

Corresponding author:
Prof. Holger B. Friedrich
School of Chemistry and Physics, University of KwaZulu-Natal, Westville Campus, Durban
4000, South Africa.
*E-mail: friedric@ukzn.ac.za
Tel: +27(0) 31 260 3107,
Fax: +27(0) 31 260 3091
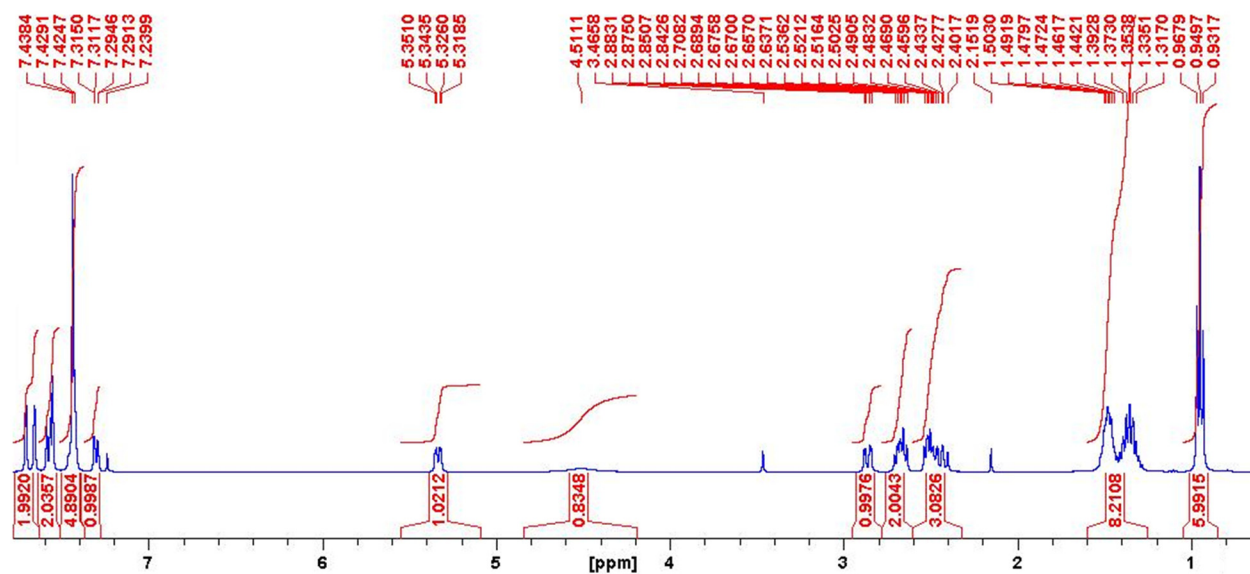
Figure 1: Proton NMR of Lumefantrine.
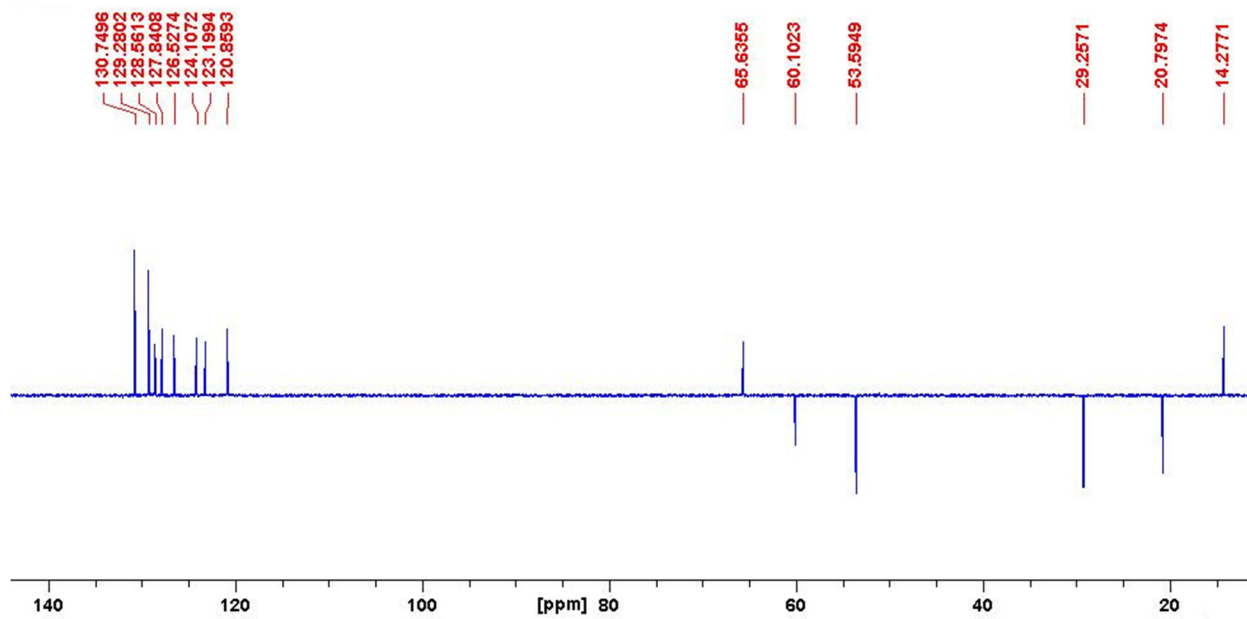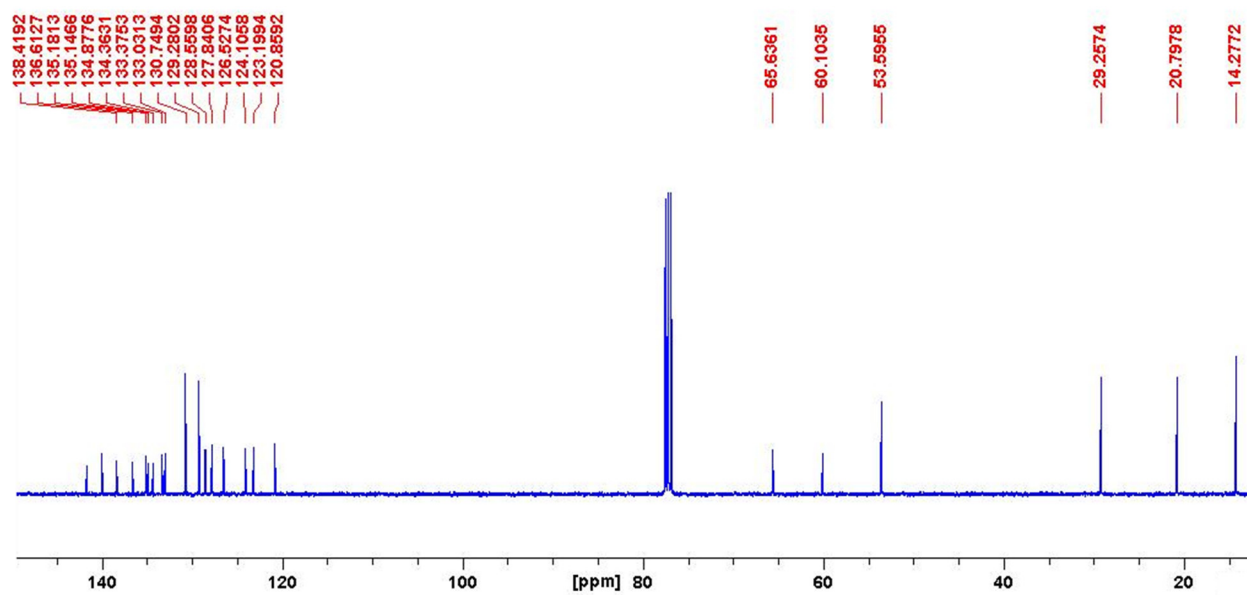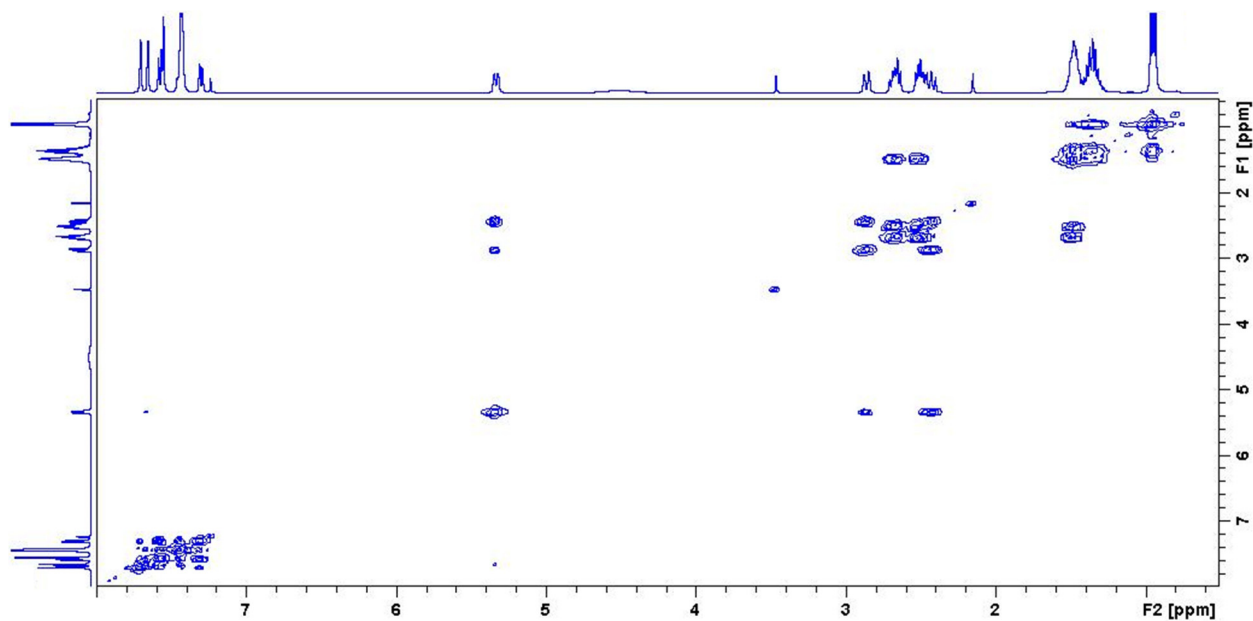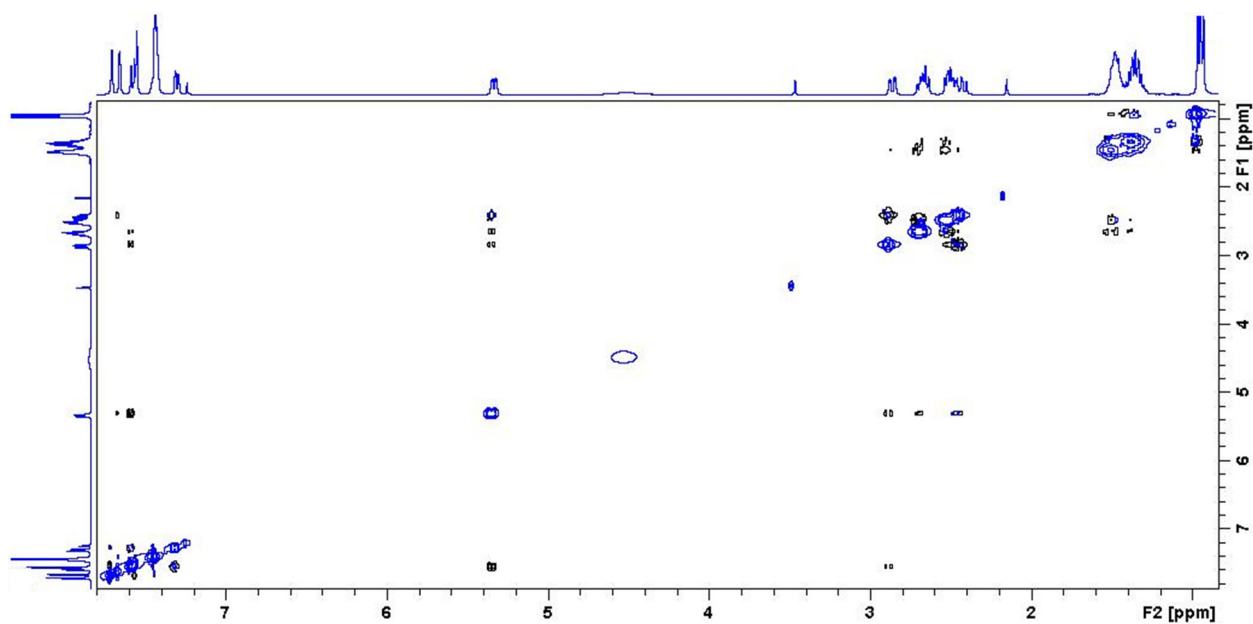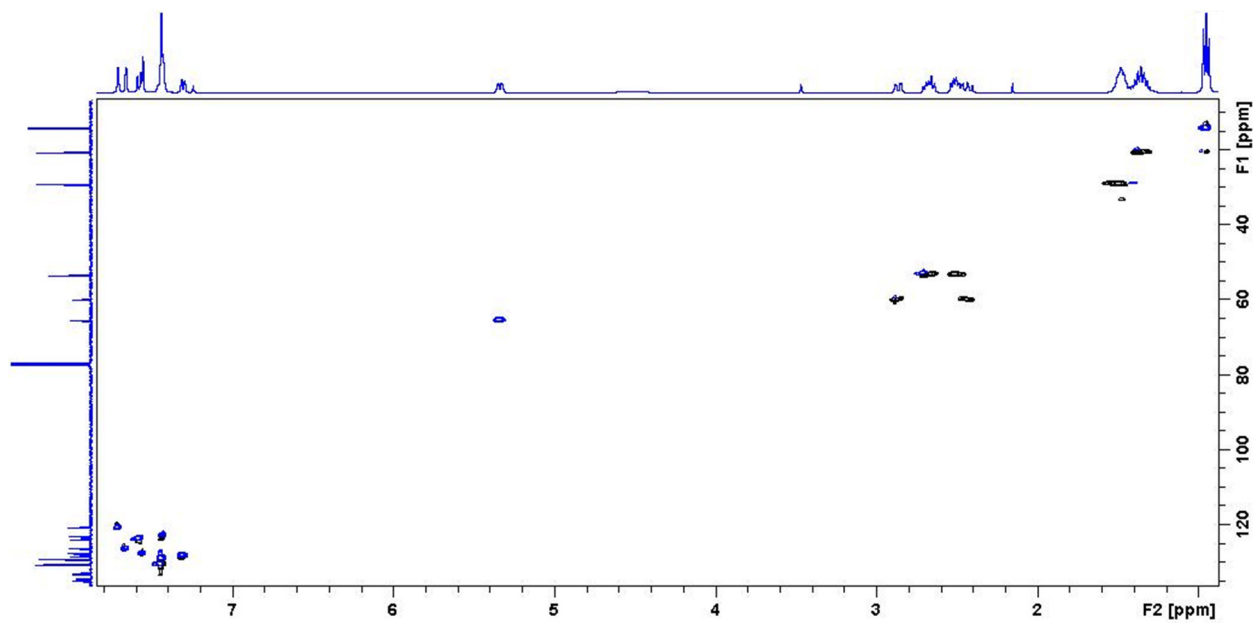
Figure 2: ^{13}C DEPT NMR of Lumefantrine.

Figure 3: ^{13}C NMR of Lumefantrine.

Figure 4: COSY NMR of Lumefantrine.

Figure 5: NOESY NMR of Lumefantrine.

Figure 6: HSQC NMR of Lumefantrine.